

ARTICLE

<https://doi.org/10.1038/s42005-019-0277-7>

OPEN

Valley phenomena in the candidate phase change material $\text{WSe}_{2(1-x)}\text{Te}_{2x}$

Sean M. Oliver ^{1,2}, Joshua Young³, Sergiy Krylyuk^{4,5}, Thomas L. Reinecke⁶, Albert V. Davydov ⁴ & Patrick M. Vora^{1,2*}

Alloyed transition metal dichalcogenides provide an opportunity for coupling band engineering with valleytronic phenomena in an atomically-thin platform. However, valley properties in alloys remain largely unexplored. We investigate the valley degree of freedom in monolayer alloys of the phase change candidate material $\text{WSe}_{2(1-x)}\text{Te}_{2x}$. Low temperature Raman measurements track the alloy-induced transition from the semiconducting 1H phase of WSe_2 to the semimetallic $1T_d$ phase of WTe_2 . We correlate these observations with density functional theory calculations and identify new Raman modes from W-Te vibrations in the 1H-phase alloy. Photoluminescence measurements show ultra-low energy emission features that highlight alloy disorder arising from the large W-Te bond lengths. Interestingly, valley polarization and coherence in alloys survive at high Te compositions and are more robust against temperature than in WSe_2 . These findings illustrate the persistence of valley properties in alloys with highly dissimilar parent compounds and suggest band engineering can be utilized for valleytronic devices.

¹Department of Physics and Astronomy, George Mason University, Fairfax, VA, USA. ²Quantum Materials Center, George Mason University, Fairfax, VA, USA. ³Department of Physics, Applied Physics and Astronomy, Binghamton University, Vestal, NY, USA. ⁴Materials Science and Engineering Division, National Institute of Standards and Technology, Gaithersburg, MD, USA. ⁵Theiss Research, La Jolla, CA, USA. ⁶Naval Research Laboratory, Washington, DC, USA. *email: pvara@gmu.edu

The valley contrasting properties of monolayer semiconducting transition metal dichalcogenides (TMDs) provide the possibility of manipulating information using the valley pseudospin^{1–3} in direct analogy to spintronics⁴. Devices that employ this schema for computation, commonly referred to as valleytronics, benefit from optical or electrical manipulation of the valley index, spin–valley locking, low power consumption, and the absence of Joule heating². These advantages have stimulated vigorous investigations into the properties of two-dimensional (2D) semiconducting TMDs with an emphasis on exploring the optical interband selection rules that connect photon polarization to valley index^{1–3}.

The first studies of monolayer TMDs focused solely on the photoluminescence (PL) from molybdenum disulfide (MoS₂)^{5,6}; however, attention shifted to valley-dependent studies^{7,8}. Soon after, monolayer tungsten diselenide (WSe₂) was found to be a superior TMD for valleytronics, exhibiting both exciton valley polarization and valley coherence^{9–15}. Valley polarization describes the probability of an exciton created in a valley to remain there until recombination, while valley coherence quantifies the probability of an exciton to remain in a superposition state of K and K' valleys before recombining. At low temperature, the neutral exciton (X⁰) in bare WSe₂ monolayers exhibits a valley polarization ranging from 40% to 70% depending on the laser energy^{9,11,16}. The depolarization of valley excitons is believed to be governed by a combination of intervalley electron–hole exchange interactions^{8,17}, phonon-assisted intervalley scattering^{7,18}, and Coulomb screening of the exchange interaction^{19,20}. In addition, WSe₂ holds the record for the largest degree of X⁰ valley coherence in bare monolayers ($\approx 40\%$ at cryogenic temperatures)⁹.

Alloying can increase the technological potential of valleytronic TMDs by combining valley contrasting properties with band engineering²¹. Furthermore, alloys of structurally distinct TMDs may also enable phase change memory technologies^{22–24} by reducing the energy barrier between semiconducting and semi-metallic states²⁵. Few studies, however, have explored valley phenomena in alloys despite the heavy interest in this field. The first exploration of valley properties in alloys focused on Mo_{1–x}W_xSe₂ at 5 K and found that there was a transition from the intrinsic valley polarization of MoSe₂ to WSe₂ as the transition metal content was varied²⁶. Experiments on a WS_{0.6}Se_{1.4} alloy demonstrated a valley polarization of $\approx 31\%$ at 14 K, which was much lower than that of both WS₂ and WSe₂²⁷. A recent study of WS_xTe_{2–x} found that the room temperature valley polarization increased from 3% in WS₂ to 37% in an unspecified alloy composition²⁸. The limited information regarding valley polarization in alloyed TMDs is a serious oversight as future valleytronic technologies will likely rely heavily on band engineering.

In this study, we examine the low-temperature optical properties of monolayer WSe_{2(1–x)}Te_{2x}, where the endpoints are the valleytronic semiconductor 1H-WSe₂ and the topological semimetal 1T_d-WTe₂. Prior studies of this alloy system were performed at 300 K and focused on unpolarized optical measurements²⁹ as well as electronic transport characterization³⁰. Our study focuses on the impact of alloying on the valley excitons of WSe_{2(1–x)}Te_{2x} monolayers encapsulated in hexagonal boron nitride (hBN). We ensure good interfacial contact in the heterostructure by cleaning with the nano-squeegee method³¹, which substantially improves the valley polarization. Raman measurements at 5 K show that increasing Te composition leads to the shifting and splitting of vibrational modes as well as the appearance of new modes unique to alloys. Polarization-resolved Raman measurements coupled with density functional theory (DFT) calculations of the theoretical 1H-WTe₂ phase allow us to assign these alloy-only features as

resulting from W-Te vibrations in the 1H WSe_{2(1–x)}Te_{2x} structure. Temperature-dependent, polarization-resolved PL measurements of the 1H-phase alloys demonstrate band gap tunability alongside the presence of new ultra-low energy emission features. We suggest that these features are from deep mid-gap states that originate from the large difference in the W-Te and W-Te bond lengths. Despite the presence of structural disorder in the lattice, valley polarization is found to survive the alloying process for $x \leq 0.14$ while valley coherence is present for alloys $x \leq 0.37$, and interestingly, we demonstrate that alloys have the ability to sustain these valley properties at higher temperatures than pure WSe₂. These findings illustrate the persistence of valley phenomena in significantly disordered alloys and point the way toward optimization of TMDs for novel phase change memories that naturally integrate with valleytronic devices.

Results

WSe_{2(1–x)}Te_{2x} structure and vibrational modes. Interpretation of our experimental data is guided by DFT modeling of the WSe_{2(1–x)}Te_{2x} phase diagram. The crystal structure of the endpoint compounds 1H-WSe₂ ($x = 0$) and 1T_d-WTe₂ ($x = 1$) are shown in Fig. 1a, b. Regarding crystal structure notation, we refer to T_d monolayers as being in the 1T_d phase. Previously, T_d and 1T' notations have been used interchangeably for T_d monolayers since the only difference between these structures in the bulk was believed to be a slight shift of layers relative to one another. Since the T_d structure contains three layers in its unit cell while the 1T'

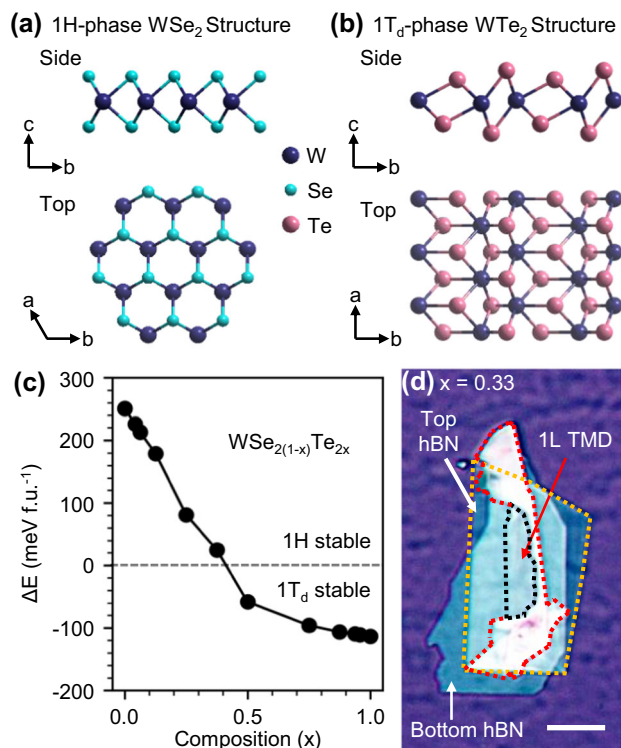


Fig. 1 Structural phases and van der Waals heterostructures of WSe_{2(1–x)}Te_{2x}. **a** Side and top view of **a** monolayer 1H-WSe₂ and **b** monolayer 1T_d-WTe₂. **c** Composition-dependent phase diagram determined from density functional theory calculations indicating a phase boundary at $x = 0.4$. **d** Optical image of a hexagonal boron nitride (hBN)-encapsulated $x = 0.33$ monolayer deposited onto a SiO₂/Si substrate. The transition metal dichalcogenide (TMD) alloy is outlined in red and the monolayer (1L) portion of that flake is outlined in black. The top layer of hBN is outlined in yellow. The white scale bar is 20 μm .

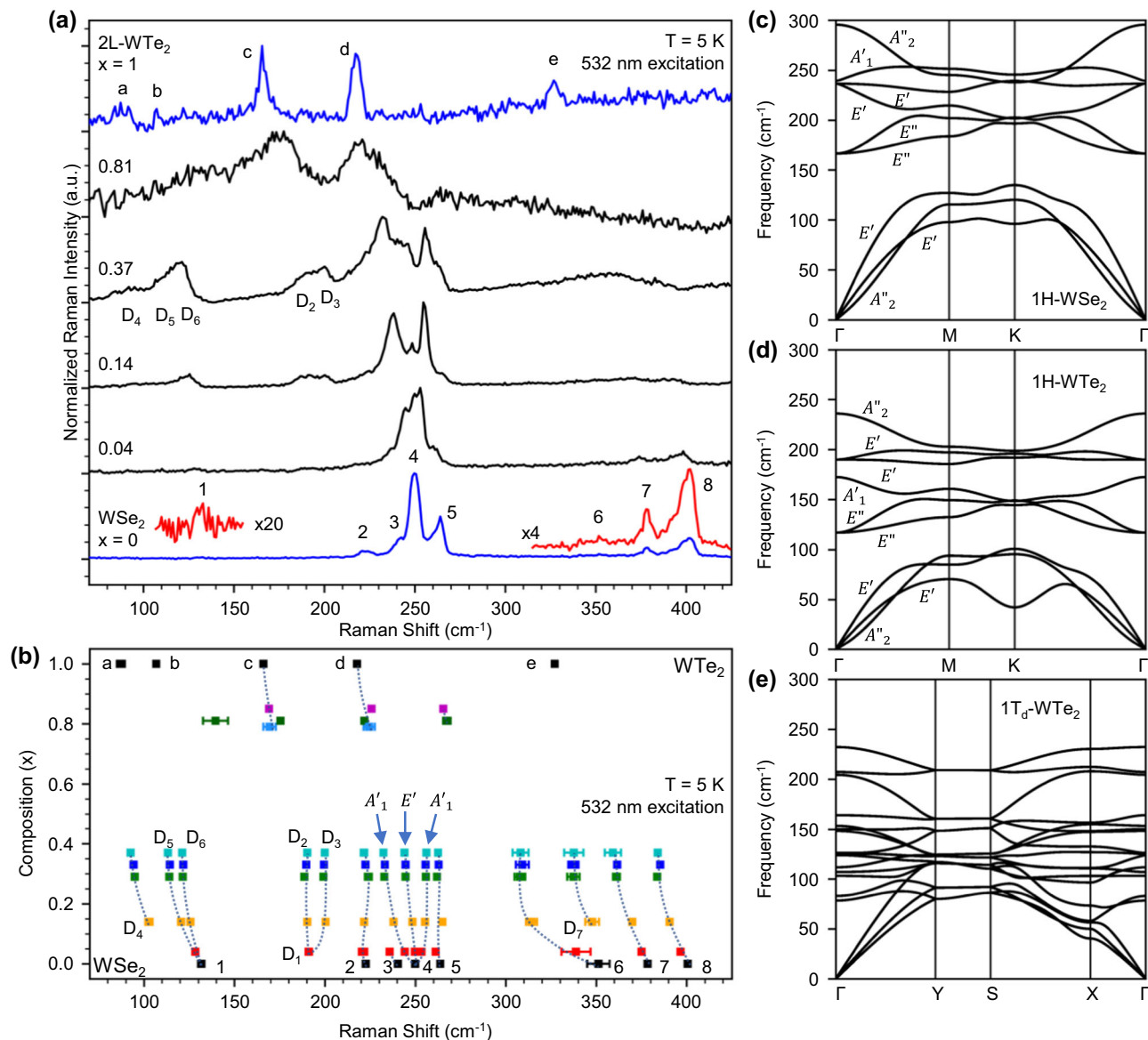


Fig. 2 Composition-dependent Raman spectra of $\text{WSe}_{2(1-x)}\text{Te}_{2x}$ and phonon band structures of WSe_2 and WTe_2 . **a** Raman measurements of monolayer WSe_2 , bilayer (2L) WTe_2 , and select monolayer $\text{WSe}_{2(1-x)}\text{Te}_{2x}$ alloys taken at 5 K with 532 nm excitation. Vibrational modes in WSe_2 and WTe_2 are identified with numbers and letters, respectively, and their assignments can be found in Table 1. Parts of the WSe_2 spectra are scaled for clarity. **b** Peak positions extracted from Raman measurements at 5 K for different alloy compositions x . Peaks identified in **a** for WSe_2 and WTe_2 are labeled with their respective numbers and letters. New alloy-induced vibrational modes are labeled D_i ($i = 1, 2, 3, \dots$). The composition-dependent shifting and the splitting of peaks are tracked with dotted lines. The error bars in **b** are one standard deviation and in most cases are smaller than the data point. **c-e** Phonon band structures calculated for 1H- WSe_2 , 1H- WTe_2 , and 1 T_d - WTe_2 .

structure contains one layer, it was assumed that monolayers isolated from a bulk T_d crystal were in the $1T'$ phase. We make the $1T_d$ notation distinction in light of a recent report which has indicated, unlike the $1T'$ phase, that inversion symmetry is broken in the monolayer T_d lattice³². We find from our DFT calculations, in agreement with previous studies^{29,30}, that the 1H phase is stable with a Te concentration of $x \leq 0.4$, which we illustrate in Fig. 1c. For $x \geq 0.5$, $1T_d$ becomes the lowest energy phase. As a result, we expect valleytronic optical properties for the 1H alloys corresponding to $x \leq 0.4$ and semimetallic behaviors for the $1T_d$ alloys $x \geq 0.5$. These predictions are consistent with our Raman and PL measurements described in detail below.

Prior to optical measurements, monolayers are encapsulated in an hBN heterostructure, as shown in Fig. 1d, to protect from the degradative effects due to exposure to the atmosphere and to

provide a uniform dielectric environment³³. We explore the effects of alloying on crystal structure through low-temperature Raman spectroscopy of hBN-encapsulated monolayer $\text{WSe}_{2(1-x)}\text{Te}_{2x}$, as shown in Fig. 2a. This Raman data is fit with multiple Lorentzian peaks to extract mode frequencies, which are plotted in Fig. 2b with alloy composition x . Examples of Lorentzian fits to Raman data for select alloys can be seen in Supplementary Fig. 1.

It is instructive to first examine the properties of the endpoints WSe_2 ($x = 0$) and WTe_2 ($x = 1$) that appear in blue in Fig. 2a. WSe_2 , which naturally crystallizes in the 1H phase, is in the D_{3h} point group and exhibits modes with A'_1 and E' symmetries. In agreement with prior observations^{34,35}, we identify eight Raman peaks in WSe_2 at 132, 223, 240, 250, 264, 351, 378, and 401 cm^{-1} . These modes and their symmetries are summarized in Table 1. The dominant feature in the WSe_2 Raman spectra at 250 cm^{-1}

Table 1 Raman mode assignments.

1H-WSe ₂		
Label	Position (cm ⁻¹)	Assignment
1	132	Unknown
2	223	$E'(K)^a$
3	240	$E'(M)^a$
4	250	$A'_1 + E'$
5	264	$2LA(M)^{a,b}$
6	351	$2E'(T)^b$ or $A'_1(M) + TA(M)^b$
7	378	$[E'(T) \text{ or } A'_1(T)] + LA(M)^{a,b}$
8	401	$[E'(T) \text{ or } A'_1(T)] + LA(K)^a$ or $3LA(M)^{a,b}$

T _d -WTe ₂ (bilayer)		
Label	Position (cm ⁻¹)	Assignment
a	87	A_2
b	107	A_2
c	166	A_1
d	218	A_1
e	327	$2A_1$ ($2 \times$ peak c) or $A_1 + A_2$ (peak d + peak b)

1H-WSe₂ and T_d-WTe₂ (bilayer) vibrational mode symmetry assignments for the peaks identified in Fig. 2a, b. WSe₂ peaks are labeled with numbers and WTe₂ peaks are labeled with letters. The superscripts a and b refer to assignments made by del Corro et al.³⁴ and Zhao et al.³⁵, respectively

(labeled peak 4 in Fig. 2a, b) is an A'_1 symmetry mode where the transition metal is fixed and the chalcogens vibrate perpendicular to the basal plane^{36,37}. In monolayer WSe₂, this mode overlaps with an E' symmetry mode where the chalcogen and transition metal layers both vibrate in plane but out of phase^{36,37}. These findings agree with prior calculations^{34,36,37} as well as our own DFT modeling of the WSe₂ phonon band structure that predicts the 0 K frequency of the dominant A'_1 mode at 239 cm⁻¹ and the E' mode at 236 cm⁻¹ (Fig. 2c). Additional monolayer WSe₂ modes are enhanced at 5 K, which are usually assigned as disorder-activated finite momentum phonons, combination modes, or difference modes^{34,35,38}. We find that previous assignments of these features to Raman difference modes conflict with our low-temperature data. Difference modes originate from a two-phonon process where one phonon is absorbed (anti-Stokes process) and another is created (Stokes process). Since this requires the presence of a phonon before photoexcitation, its occurrence is expected to follow a Boltzmann-like temperature dependence that disappears at cryogenic temperatures³⁹. The presence of these so-called difference modes in our measurements at 5 K calls this assignment into question. Thus it is more likely that these features are combination modes for which there are many possible assignments (Table 1); however, there is presently no explanation for the mode at 132 cm⁻¹.

We now discuss the Raman spectrum of WTe₂, which is presented in Fig. 2a. Our attempts to exfoliate large-area monolayers of WTe₂ were met with limited success, which may be due to the rapid oxidation rate of this material⁴⁰. In contrast, we found it straightforward to achieve large-area bilayer WTe₂, which is known to be less susceptible to oxidation⁴⁰. The Raman spectra of bilayer and monolayer WTe₂ are nearly identical⁴¹, which lets us safely use bilayer WTe₂ to discriminate between 1T_d- and 1H-WSe₂(1-x)Te_{2x}. Bilayer WTe₂ (T_d phase) belongs to the C_{2v} point group, and so only A_1 and A_2 symmetry modes can be observed⁴². Five peaks in the 70–425 cm⁻¹ range are present at 87, 107, 166, 218, and 327 cm⁻¹ and are labeled with letters in Fig. 2a, b. Assignment of the mode symmetries is based on prior studies of WTe₂^{41,43} and is included in Table 1. The feature at 327 cm⁻¹, labeled peak e, has not been previously observed, and we assign it as either a second-order

overtone of the 166 cm⁻¹ A_1 mode (peak c) or a combination of the 107 cm⁻¹ A_2 and 218 cm⁻¹ A_1 modes (peaks b and d, respectively).

Low-temperature Raman measurements of the alloys (black curves of Fig. 2a) reveal fascinating new details regarding the vibrational modes that were not observed in a previous study of WSe₂(1-x)Te_{2x} alloys²⁹ owing to thermal broadening at 300 K (see Supplementary Fig. 2 for comparison of 5 and 300 K spectra). Alloys with $x \leq 0.37$ are in the 1H phase, which is further supported by the presence of PL in these samples to be discussed later, and exhibit complex mode structures in the ≈ 230 –275 cm⁻¹ range. Polarization-resolved Raman measurements (Supplementary Fig. 3) reveal that the dominant WSe₂ A'_1 mode at 250 cm⁻¹ splits into two peaks at 244 and 253 cm⁻¹ for $x = 0.04$ (see red points in Fig. 2b). This differs from studies of WS₂(1-x)Se_{2x} where this primary out-of-plane WSe₂ feature typically only shifts with alloying^{44,45}. The splitting of out-of-plane vibrational modes with alloying, however, has been seen in MoS_xSe_{2-x} monolayers^{46,47} and has been carefully documented in few-layer MoS_xSe_{2-x}⁴⁸. Jadczyk et al. attributed the splitting of this feature in alloys to the polarization of the alloy unit cell due to the substitution of heavier chalcogens that introduce different force constants in the lattice⁴⁸. Thus, owing to the splitting of the primary A'_1 mode, we find that the E' mode is distinguishable from the A'_1 mode in alloy monolayers and only slightly shifts to lower frequencies with increasing x .

Several other WSe₂-like vibrational modes show sensitivity to alloying for 1H-phase compositions $x \leq 0.37$. Second-order finite momentum peaks 6, 7, and 8 of Fig. 2a, b shift to lower frequencies and broaden with increasing alloy composition. This alloy data may clarify disagreements in the literature on whether A'_1 or E' phonons are the dominant contributor to these higher-order modes^{34,35}. The band predictions of 1H-WSe₂ in Fig. 2c show both branches of the E' mode that originate at 236 cm⁻¹ shift to lower frequencies away from the Γ point. This behavior is opposite to that of the A'_1 mode, which originates at 239 cm⁻¹ and shifts to higher frequencies away from the Γ point. Since peaks 6, 7, and 8 broaden asymmetrically on the lower frequency side of their centers as x is increased, this may indicate that the E' mode, rather than the A'_1 mode, contributes to these higher-order processes. The shifting and broadening of the WSe₂ modes for compositions $x \leq 0.37$ indicate that alloying introduces significant disorder into the lattice but globally maintains the 1H phase.

A particularly interesting alloy-induced feature resolved in 1H samples is the Raman peak labeled D₁ at 191 cm⁻¹ in $x = 0.04$ (red points in Fig. 2b). This feature splits into the two peaks labeled D₂ and D₃ at 190 and 200 cm⁻¹, respectively, as x is increased. Polarization-resolved Raman measurements (Supplementary Fig. 3) indicate that these features have A'_1 symmetry and DFT calculations of the 1H-WSe₂ phonon band structure (Fig. 2c) show no A'_1 phonon modes present in this range. We therefore calculate the phonon band structure of metastable 1H-WTe₂ phase in Fig. 2d, which predicts an A'_1 Γ -point mode at 172 cm⁻¹. This mode is the closest to the observed results and so we assign the D₁ peak to an A'_1 mode arising from W-Te vibrations in the 1H WSe₂(1-x)Te_{2x} alloys. We attribute its splitting to increasing force constant variations introduced into the lattice with noticeable Te content as discussed previously for the primary A'_1 mode of WSe₂⁴⁸. Raman measurements reveal several other new peaks in the 1H alloys, which we label D₄, D₅, D₆, and D₇ in Fig. 2b. These polarization-independent features (see Supplementary Fig. 3) most likely arise from either finite momentum WSe₂-like phonons or WSe₂ combination modes. We exclude difference modes based on the use of low-temperature spectroscopy as discussed previously. Possible assignments are $E'(M)$ for D₆ and $E' + E'(M)$ for D₇, while D₄ and D₅ remain unassigned but may originate from combinations of 1H-WSe₂ and 1H-WTe₂ modes.

As $\text{WSe}_2(1-x)\text{Te}_2x$ transitions to the 1T_d phase with alloying, the Raman spectra for $x \geq 0.79$ show the two primary A_1 vibrational modes of pure WTe_2 , labeled peaks c and d in Fig. 2a, b. These features are shifted and broadened due to alloy disorder in agreement with other WTe_2 alloys⁴⁹. The phonon band structure of $1\text{T}_d\text{-WTe}_2$ is shown in Fig. 2e for comparison with that of 1H-WTe_2 in Fig. 2d.

Excitonic properties. In Fig. 3a–e, we present temperature-dependent PL spectra for representative 1H-phase alloys. Each spectrum has been normalized by the maximum intensity and was excited with right circularly polarized light ($\sigma+$) at 1.96 eV. The

collected PL is passed through a waveplate/analyzer combination to select $\sigma+$ emission. At 300 K, the PL spectra show contributions from both the neutral exciton (X^0) and the trion (X^T)¹². Increasing the Te concentration causes both features to redshift due to the lower band gap of 1H-WTe_2 ⁵⁰. As temperature decreases from 300 to 5 K, X^0 and X^T sharpen, blueshift, and weaken in intensity. The latter behavior is due to the sign of the conduction band spin–orbit coupling, which makes the lowest exciton state dark⁵¹. The sign of the spin–orbit coupling is the same for all W-based TMDs⁵¹ and so we expect no change in the optical activity of the lowest exciton state with Te substitution. The presence of broad features at lower energies compared to X^0 and X^T originate from a combination of higher-order excitonic complexes⁵² and localized exciton

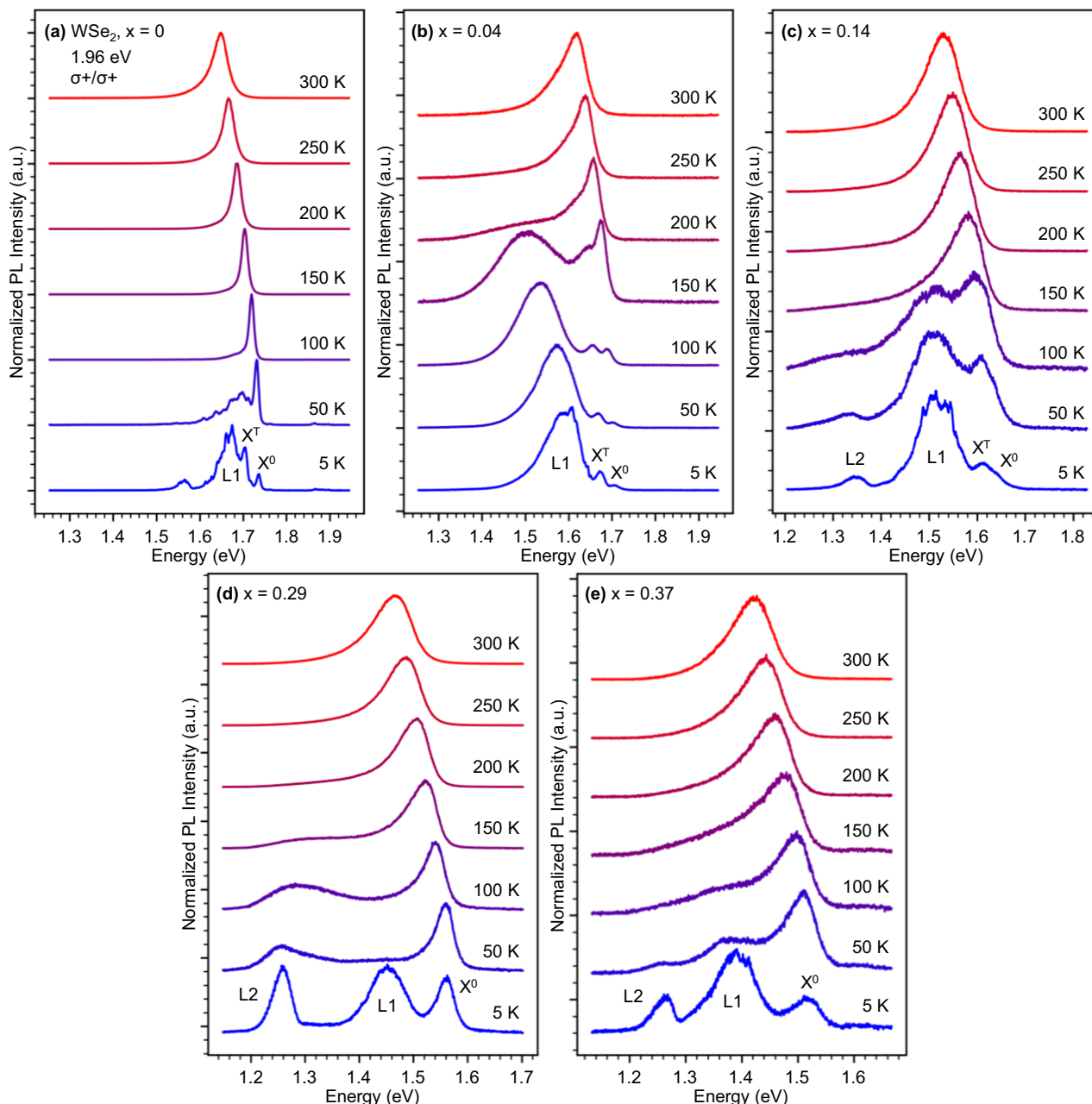


Fig. 3 Temperature-dependent photoluminescence (PL) of $1\text{H-WSe}_2(1-x)\text{Te}_2x$. PL measurements (1.96 eV excitation) of **a** WSe_2 , as well as 1H-phase $\text{WSe}_2(1-x)\text{Te}_2x$ alloys corresponding to **b** $x = 0.04$, **c** $x = 0.14$, **d** $x = 0.29$, and **e** $x = 0.37$. Excitation and collection are done with right circularly polarized light ($\sigma+$). The neutral exciton (X^0) and trion (X^T) are labeled where appropriate. Emission at 300 K is dominated by X^0 , which has a low-energy tail resulting from the presence of X^T . As the temperature is decreased, X^0 and X^T sharpen and blueshift while the localized exciton features L1 and L2 begin to dominate the spectra.

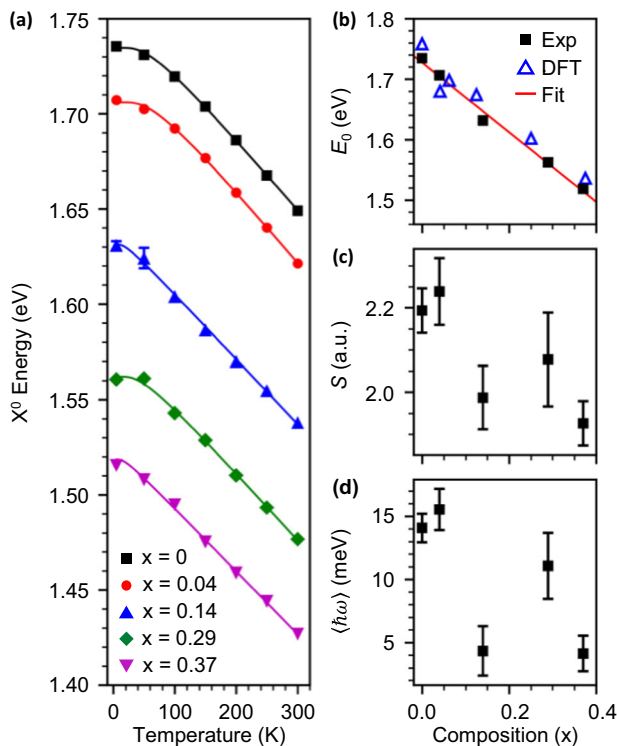


Fig. 4 Composition- and temperature-dependent exciton energies.

a Neutral exciton (X^0) energies extracted from temperature-dependent photoluminescence measurements (1.96 eV excitation). Excitation and collection are done with right circularly polarized light. The solid lines are fits to Eq. (1). The compositional dependence of the extracted parameters E_0 , S , and $\hbar\omega$ are plotted in **b–d**, respectively. E_0 is found to be tunable with alloying, while S and $\hbar\omega$ are found to decrease with increasing alloy composition x . In **b**, we plot density functional theory (DFT)-predicted optical band gaps as blue triangles, while the red curve is a fit to a line used to extract a 0-K band gap for 1H-WTe₂ of 1.15 eV. Error bars shown in all panels are equal to one standard deviation.

states from lattice defects, strain, and residual impurities introduced during fabrication^{9,12,53}.

We explore band gap tunability of 1H-WSe₂(1- x)Te_{2 x} by extracting X^0 energy as a function of temperature, which is plotted in Fig. 4a. This data is fit with a semi-empirical formula for temperature-dependent optical band gaps given by⁵⁴

$$E_g(T) = E_0 - S\langle\hbar\omega\rangle \left[\coth\left(\frac{\langle\hbar\omega\rangle}{2kT}\right) - 1 \right] \quad (1)$$

where E_0 is the gap at absolute zero, S is a dimensionless electron-phonon coupling parameter, $\hbar\omega$ is an average phonon energy, and k is the Boltzmann constant. This formula models the reduction in band gap with increasing temperature due to a combination of increasing lattice constants and exciton-phonon coupling⁵⁴. Fits of Eq. (1) to our data are presented as solid lines in Fig. 4a and the compositional dependence of E_0 , S , and $\hbar\omega$ from these fits are plotted in Fig. 4b–d. Figure 4b shows that E_0 (i.e., X^0 energy) varies in 1H-WSe₂(1- x)Te_{2 x} from ≈ 1.735 eV in WSe₂ to ≈ 1.519 eV in the $x = 0.37$ alloy. These experimental results agree extremely well with the optical band gaps of the alloys computed using DFT with the HSE06 exchange-correlation functional^{55,56}, which predict a gap of 1.75 eV in 1H-phase WSe₂ that decreases to 1.53 eV at a Te concentration of $x = 0.375$ (blue triangles of Fig. 4b). At higher x , the system transforms to the 1T_d phase (Supplementary Fig. 4), which is a semimetal.

For a comparison of DFT results for the optical band gaps of all WSe₂(1- x)Te_{2 x} monolayers calculated using both the HSE06 and Perdew–Burke–Ernzerhof (PBE) functionals and the density of states determined using the HSE06 functional, see Supplementary Fig. 4. Since the alloys are in the 1H phase only up to $x = 0.37$ and 1H-WTe₂ does not exist in nature, we are unable to reliably determine the bowing parameter for E_0 ²¹. Therefore, we instead fit E_0 from $x = 0$ to 1 with a linear function as shown by the red line in Fig. 4b. From a linear extrapolation to $x = 1$, we determine the 0 K optical band gap of 1H-WTe₂ to be 1.15 eV. Lastly, extracted values for S range from 1.93 to 2.24 and for $\hbar\omega$ between 4 and 16 meV (32.3–129 cm⁻¹) and are plotted versus x in Fig. 4c, d.

Elaborating on the 5 K PL spectra of Fig. 3, we find that X^T appears ≈ 30 meV below X^0 in our data and shifts in lockstep with the neutral exciton so that there is only weak dependence of the X^0 - X^T binding energy on x (Supplementary Fig. 5). Spatial PL mapping of an $x = 0.33$ alloy sample at 5 K indicates little variation of the intensities, energies, and line widths of X^0 and X^T . These maps are discussed in detail in Supplementary Note 1 and Supplementary Fig. 6. In addition, we find evidence for excitonic transitions and exciton-phonon complexes at energies above X^0 known to originate from coupling between hBN and WSe₂ in van der Waals heterostructures^{57,58}. A detailed discussion of these features is presented in Supplementary Note 2 and Supplementary Fig. 7. In 5 and 300 K reflectance measurements presented in Supplementary Fig. 8, both the A and B excitons are clearly visible and the valence band spin-orbit coupling is found to increase with Te incorporation.

Localized excitons are common in W-based TMDs owing to the long lifetime of the dark exciton ground states. We identify such features in all alloys and the parent compound WSe₂, beginning with an emission band ≈ 100 meV below X^0 hereafter referred to as L1. For all $x > 0.04$, L1 is accompanied by a second localized emission feature (L2) approximately ≈ 300 meV below X^0 (Fig. 3c–e). This feature has never been observed in TMDs, alloyed or otherwise. L1 and L2 maintain a similar energy separation with respect to X^0 at all nonzero x but do exhibit variations in their temperature-dependent behaviors.

The new defect band L2 must originate from a disorder unique to Te-rich alloys and may be connected to the preference of WTe₂ to crystallize in a 1T_d structure. Scanning tunneling electron microscopy measurements and molecular dynamics (MD) simulations of a similar alloy system, WS₂-Te_{2 x} ⁵⁹, indicate that Te substitution at levels approaching 15% can substantially modify the structure of a 1H-phase alloy. The bond lengths and lattice constants of 1H-WSe₂ with 1H-WTe₂ are predicted to differ by ≈ 7 –8%⁵⁹, which also leads to a mismatch between the metal-chalcogen bond angles. MD simulations presented by Tang et al.⁵⁹ illustrate that these internal strains can lead to the displacement of Te atoms from the expected chalcogen site for concentrations as low as 8%. These shifts lead to the compression and stretching of neighboring hexagonal rings and in turn result in the displacement of the native chalcogen and even the W atoms. For the WS₂-WTe₂ alloys, continuing to increase the Te doping to 15%, 20%, and finally 25% increased the displacements of W, S, and Te atoms and ultimately drove the W atoms closer together in a prelude to the 1H-1T_d transition⁵⁹. These Te concentrations compare favorably with the values at which we observe the presence of the L2 feature (Fig. 3). The presence of such substantial atomic displacements and internal strains seems to be unique to TMD alloys that are mixtures between different structural phases. We therefore suggest that the internal strains driven by Te incorporation in 1H-phase alloys create a new band of defect states (i.e., the L2 feature) lower than those typically expected from chalcogen or transition metal vacancies (i.e., the L1 feature)⁵³.

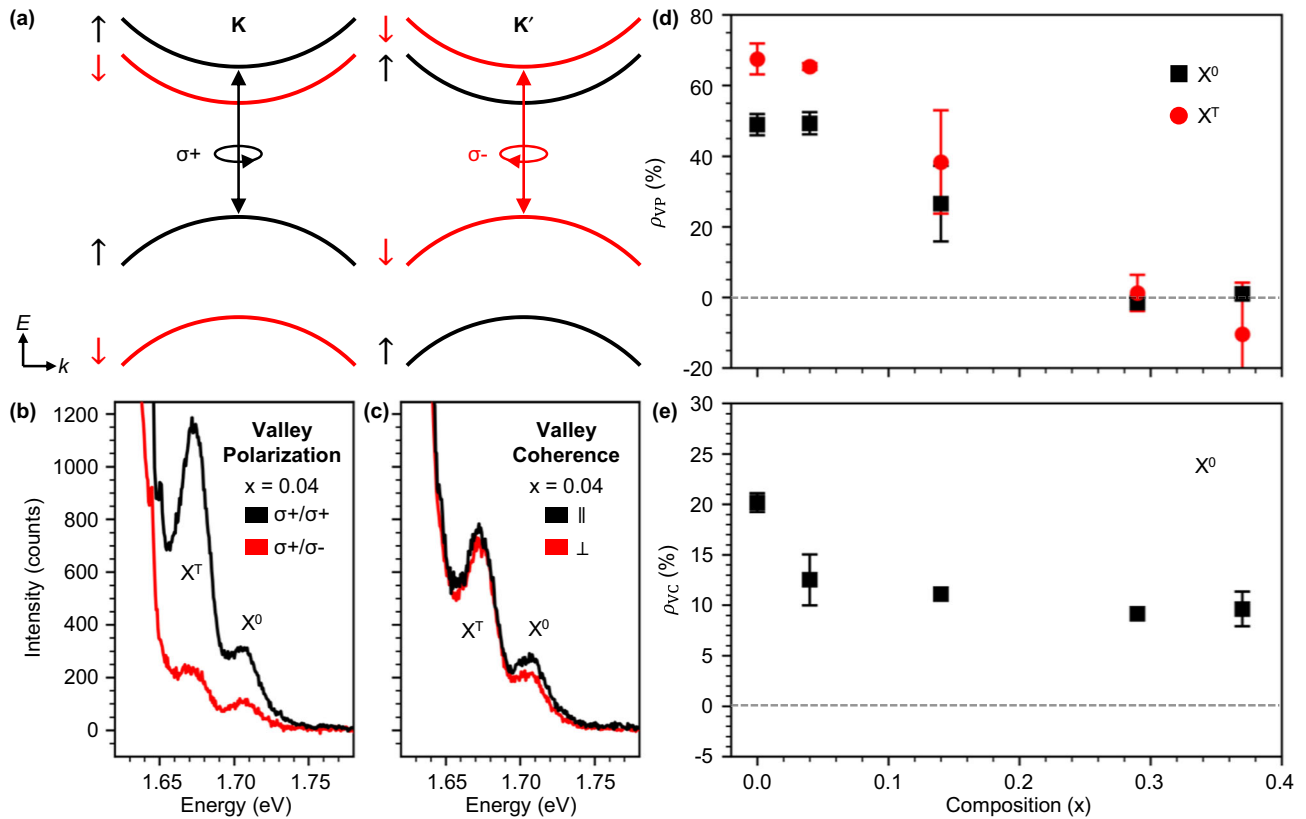


Fig. 5 Valley properties of $\text{WSe}_2(1-x)\text{Te}_x$ at 5 K. **a** Simplified image of the electron bands near the K and K' points of the hexagonal Brillouin zone in monolayer WSe_2 . Valley-dependent optical selection rules couple transitions at the K (K') valleys with $\sigma+$ ($\sigma-$) circularly polarized light. **b, c** show example spectra of valley polarization and valley coherence measurements for $x = 0.04$, respectively. **d** The degree of valley polarization (ρ_{VP}) of the neutral exciton (X^0 , black squares) and the trion (X^T , red circles) and **e** the degree of valley coherence (ρ_{VC}) of X^0 plotted against alloy composition x . The error bars shown in **d, e** are equal to one standard deviation.

Valley phenomena. Next, we explore valley contrasting in 1H- $\text{WSe}_2(1-x)\text{Te}_x$ alloys at 5 K using 1.96 eV excitation with $\sigma+$ polarization. The schematic band structure in Fig. 5a illustrates the spin-valley polarized selection rules in WSe_2 , where transitions between the valence band and the second highest conduction band are $\sigma+$ ($\sigma-$) polarized at the K (K') point. Any emission in the opposite polarization channel is a sign of intervalley scattering. Valley polarization is determined by measuring co- and cross-polarized PL spectra in the circular basis as shown in Fig. 5b. The degree of valley polarization ρ_{VP} for $\sigma+$ excitation is defined as $\rho_{VP} = (I_{\sigma+} - I_{\sigma-}) / (I_{\sigma+} + I_{\sigma-})$, where $I_{\sigma+}$ ($I_{\sigma-}$) is the intensity of the collected light with $\sigma+$ ($\sigma-$) orientation. Valley coherence measurements are similar except measurements are carried out in a linear basis with co-polarized (\parallel) and cross-polarized (\perp) configurations as shown in Fig. 5c. The degree of valley coherence ρ_{VC} is calculated similarly as $\rho_{VC} = (I_{\parallel} - I_{\perp}) / (I_{\parallel} + I_{\perp})$, where I_{\parallel} (I_{\perp}) is the intensity of the collected light that is \parallel (\perp) to the incident light.

Alloy-dependent values of ρ_{VP} for X^0 (black squares) and X^T (red circles) at 5 K are plotted in Fig. 5d. We find that $\rho_{VP} \approx 49\%$ for X^0 in WSe_2 , which agrees with previously reported values⁹. Achieving this value required cleaning our heterostructures post-assembly using the nano-squeegee technique³¹. This process improved the WSe_2 ρ_{VP} of X^0 by a factor of ≈ 1.7 , thus increasing the signal from 29% to 49%, whereas it appeared to have very little effect on ρ_{VC} . This result illustrates the impact of contaminants on valley properties and a comparison of squeegeed and non-squeegeed alloys can be found in Supplementary Fig. 9.

As Te is substituted into the lattice, ρ_{VP} first remains unchanged at $x = 0.04$ and then decreases to 32% at $x = 0.14$ (Fig. 5d). For $x > 0.14$, no valley polarization is observed. X^T exhibits a similar trend with x : $\rho_{VP} \approx 67\%$ for X^T in WSe_2 and is zero for $x > 0.14$. To the best of our knowledge, there is no systematic theory for understanding valley depolarization from alloy disorder. However, we do observe an interesting correlation between ρ_{VP} and the integrated intensity ratio of X^T/X^0 , as shown in Supplementary Fig. 10. The $\rho_{VP} X^T/X^0$ integrated intensity ratio generally decreases with Te incorporation from ≈ 2.4 in WSe_2 to ≈ 0.25 in $x = 0.37$. While there is an initial increase in the $\rho_{VP} X^T/X^0$ intensity ratio from ≈ 2.4 in WSe_2 to ≈ 3.8 in the $x = 0.04$ sample, this is most likely the result of a superior cleaned interface via the nano-squeegee method rather than an intrinsic material property. The decrease in the $\rho_{VP} X^T/X^0$ intensity ratio as x is increased suggests a connection between ρ_{VP} and an apparent reduction in doping with increasing Te substitution. Valley coherence is only present for neutral excitons⁹ and we plot ρ_{VC} versus x at 5 K in Fig. 5e. $\rho_{VC} \approx 20\%$ in WSe_2 , which is slightly lower than the literature value⁹, and decreases to $\approx 13\%$ when $x = 0.04$ after which point it remains essentially constant until the 1H-1T_d phase transition. We note that valley coherence remains finite even when valley polarization goes to zero at large x .

Temperature-dependent measurements of ρ_{VP} and ρ_{VC} for X^0 in Fig. 6 show interesting behaviors that suggest disorder can in some cases improve valley polarization and valley coherence. In all cases for the 1H-phase alloys, we find a decrease of both quantities with increasing temperature. However, alloys exhibit a different temperature dependence when compared to WSe_2

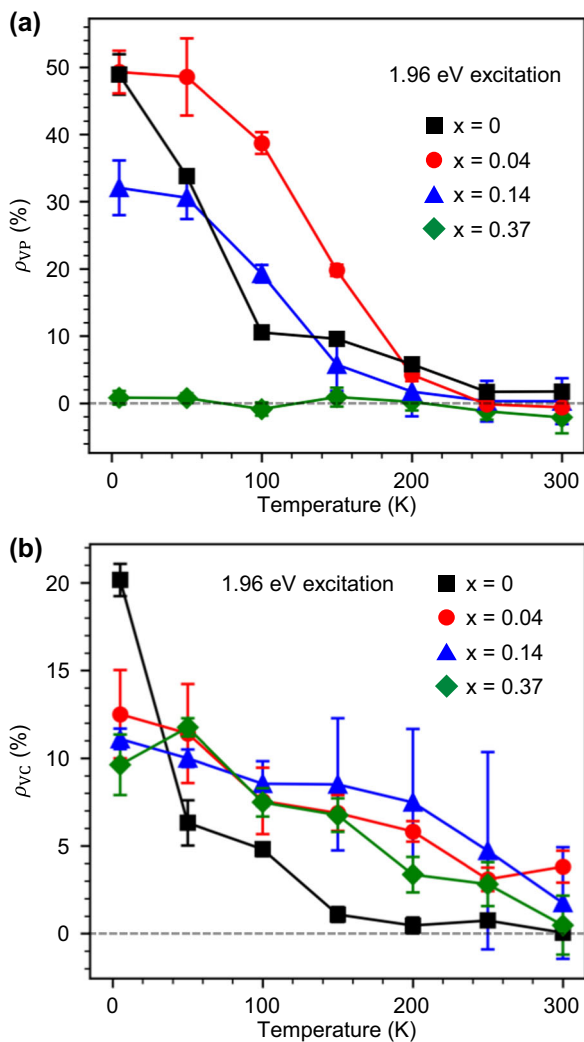


Fig. 6 Temperature dependence of the degree of valley polarization (ρ_{VP}) and the degree of valley coherence (ρ_{VC}) in 1H-WSe₂(1-x)Te_{2x}. **a** ρ_{VP} and **b** ρ_{VC} of 1H-WSe₂(1-x)Te_{2x} as a function of temperature. In both cases, the alloys are found to sustain valley properties at elevated temperatures when compared to pure WSe₂ ($x = 0$). Measurements in both panels are done with 1.96 eV excitation. The solid lines are guides to the eye and the error bars are equal to one standard deviation.

($x = 0$). Beginning with ρ_{VP} in Fig. 6a, we observe a sharp decrease with increasing temperature that is consistent with prior examinations of WSe₂ monolayers^{12,60}. Surprisingly, we find that valley polarization remains large for the $x = 0.04$ alloy and can exceed that of WSe₂, reaching a maximum enhancement factor of 3.5 \times at 100 K. While valley polarization is overall lower for the $x = 0.14$ alloy, it also exceeds that of WSe₂ at 100 K and has the same temperature dependence as the $x = 0.04$ case. We note that ρ_{VP} of X^T also shows similar temperature and alloy dependence, which can be seen in Supplementary Fig. 11. This observation indicates that, counter to intuition, alloys can exhibit valley polarization that meets or exceeds that of WSe₂, especially at higher temperatures.

Currently, there is no systematic understanding of the impact of alloy disorder on valley polarization. The prevailing theories of valley polarization revolve around a balance between the mean exciton lifetime τ_x and the valley relaxation lifetime τ_v , which are parametrized by the relationship $\rho_{VP} = \frac{\rho_0}{1+2(\gamma_v/\gamma_x)}$, where $\gamma_v = (2\tau_v)^{-1}$ is the intervalley scattering rate and $\gamma_x = (\tau_x)^{-1}$ is the

exciton recombination rate^{8,19}. Temperature dependence enters this equation via the scattering and recombination rates, and the valley depolarization rate for excitons is determined by a combination of electron-hole exchange interactions^{8,17}, intervalley phonon scattering^{7,18}, and Coulomb screening⁶¹ of the exchange interaction. Miyauchi et al.¹⁹ more deeply explore the temperature dependence of τ_v and find that valley depolarization at low temperatures is driven by long-range electron-hole exchange interactions, but as temperatures are increased, intervalley phonon scattering dominates. A subsequent experimental study demonstrated that the valley polarization can be enhanced over a range of temperatures by electrostatic gating, which adds additional carriers to the material that screen the electron-hole exchange interaction²⁰. Therefore, we suggest that carrier doping may be a contributing factor to the enhancement of ρ_{VP} in alloys at elevated temperatures, which is supported by the larger X^T/X⁰ integrated intensity ratio for $x = 0.04$ compared to WSe₂ (Supplementary Fig. 10). However, we cannot conclude that doping is the only factor since the X^T/X⁰ integrated intensity ratio of the $x = 0.14$ alloy is less than that of WSe₂ but its valley polarization is larger at 100 K. Another possible explanation for the sustained valley polarization at higher temperatures may be a reduction in τ_x due to disorder⁶². We have attempted to fit our data using functional forms provided by Miyauchi et al.¹⁹ but cannot obtain unique fitting parameters since both τ_x and τ_v are complicated functions of temperature, bright-dark exciton splitting, phonon scattering rates, and exciton relaxation times.

The valley decoherence rate differs from the valley depolarization rate by its additional sensitivity to pure dephasing (γ_{dep}). This results in a different expression $\rho_{VC} = \frac{\rho_0}{1+2(\gamma_v+\gamma_{dep})/\gamma_x}$ ^{63,64}. Unique temperature dependencies for ρ_{VP} and ρ_{VC} are therefore expected and observed in Fig. 6a and Fig. 6b, respectively. We again find that for alloys the valley coherence is larger than in WSe₂ at higher temperatures. The impact of pure dephasing on valley coherence makes it more sensitive to scattering events than valley polarization. According to Hao et al.¹¹, changes in exciton momentum due to scattering from defects yields an in-plane magnetic field that leads to depolarization and decoherence. As the frequency of impurity scattering is increased, however, the time-averaged effective magnetic field experienced by excitons due to the electron-hole exchange interaction¹⁷ is reduced, which can act to enhance valley properties. Further studies on WSe₂(1-x)Te_{2x} using temperature-dependent and time-resolved spectroscopies such as those conducted by Miyauchi et al.¹⁹ and Hao et al.¹¹ are required to determine the respective contributions of the above decoherence and depolarization mechanisms.

Discussion

We have used low-temperature Raman and temperature-dependent, polarization-resolved PL spectroscopy to characterize different crystal phases spanned by monolayer WSe₂(1-x)Te_{2x} alloys and explore how incorporation of Te into the WSe₂ lattice affects valleytronic and semiconducting properties. DFT calculations of the phonon dispersion curves for 1H-WSe₂ and 1T_d-WTe₂ alongside low-temperature Raman measurements allowed us to assign the vibrational modes of the WSe₂ and WTe₂ endpoint compounds. The shifting and splitting of these vibrational modes were tracked with composition x , and we found the appearance of alloy-only features resulting from W-Te vibrations in the 1H alloys that we confirm through the combination of polarization-resolved Raman measurements and DFT calculations. Temperature-dependent PL measurements were used to demonstrate band gap tunability, identify the alloy dependence of exciton and trion states, and observe a new defect-related emission feature. DFT calculations of the optical band gap in the alloys agree very well with low-

temperature PL measurements when using the HSE06 functional. Polarization-resolved PL measurements show that alloys still exhibit valley polarization and coherence and that these valley properties can be superior to those of WSe_2 at higher temperatures. Reflectance measurements were also used to measure the A and B excitons in select alloys, indicating that the spin-orbit splitting of the valence band can be increased with the addition of Te. This study illustrates the resilience of valley phenomena in alloys and the prospect of their application in a novel class of phase change memory technologies that also take advantage of spintronic and valleytronic information processing.

Methods

Crystal growth and structural characterization. $\text{WSe}_{2(1-x)}\text{Te}_{2x}$ alloys ($x = 0 \dots 1$) were grown by the chemical vapor transport method. Appropriate amounts of W (99.9%), Se (99.99%), and Te (99.9%) powders were loaded in quartz ampoules together with ≈ 90 mg (≈ 4 mg/cm³ of the ampoule's volume) of TeCl_4 which served as a transport agent. The ampoules were then sealed under vacuum and slowly heated in a single-zone furnace until the temperature at the source and the growth zones reached 980 and 830 °C, respectively. After 4 days of growth, the ampoules were ice-water quenched. Crystal phases of the alloys were determined by examining powder X-ray diffraction patterns using the MDI-JADE 6.5 software package. We found that alloys with $x \leq 0.4$ crystallized in the 2H phase and those with $x \geq 0.8$ were in the T_d phase. Results are consistent with a previous report of $\text{WSe}_{2(1-x)}\text{Te}_{2x}$ ²⁹. Chemical compositions were determined by the energy-dispersive X-ray spectroscopy (EDS) using a JEOL JSM-7100F field-emission scanning electron microscope equipped with an Oxford Instruments X-Max 80 EDS detector.

Sample preparation. For optical studies, $\text{WSe}_{2(1-x)}\text{Te}_{2x}$ bulk crystals were mechanically exfoliated and monolayers were identified by optical contrast. Monolayers were then fully encapsulated in an hBN heterostructure (top and bottom layers) using the viscoelastic dry-stamping method on a SiO_2/Si substrate (90 nm oxide thickness) to protect them from the degradative effects due to exposure to the atmosphere and to provide a uniform dielectric environment³³. We note that, before encapsulation, monolayers were exposed to the atmosphere for <1 h. To guarantee clean hBN/TMD contact, the nano-squeegee method was used with a scan line density of ≥ 10 nm/line and a scan speed of ≤ 30 $\mu\text{m/s}$ as suggested by Rosenberger et al.³¹ to physically push contaminants out from in between heterostructure interfaces. Results of this procedure can be seen in the atomic force microscopic image of Supplementary Fig. 6. Here the contaminants removed from the interfaces are gathered along both sides of the nano-squeegee region (dark vertical lines, ≈ 50 nm in height above sample).

Optical studies. Raman and PL measurements were performed on home-built confocal microscopes, both in backscattering geometries, that were integrated with a single close-cycle cryostat (Montana Instruments Corporation, Bozeman, MT). A 532 nm laser was used for Raman measurements since it has been shown that this excitation source can excite first- and second-order features³⁴, whereas a 633 nm laser was used for PL measurements since it has been shown to yield a much higher degree of valley polarization than excitation with a green laser¹⁶. Both set-ups focus the excitation source through a 0.42 NA long working distance objective with $\times 50$ magnification. For Raman measurements, the laser spot was ≈ 2.4 μm , and the laser power density was fixed at 66 $\mu\text{W}/\mu\text{m}^2$, while for PL measurements, the laser spot was determined to be ≈ 2.2 μm , and the laser power density was fixed at 21 $\mu\text{W}/\mu\text{m}^2$. Collected light in both cases was directed to a 500 nm focal length spectrometer with a liquid nitrogen-cooled CCD (Princeton Instruments, Trenton, NJ). The spectrometer and camera were calibrated using a Hg-Ar atomic line source. For spectral analysis, Raman peaks were fit with Lorentzian profiles, whereas PL peaks were fit with Gaussians.

DFT calculations. DFT calculations were performed using the Vienna ab initio Simulation Package^{65–67}. Projector augmented wave pseudopotentials⁶⁸ and the PBE exchange-correlation functional⁶⁵ were utilized. Spin-orbit coupling was included in all calculations except for the phonon band structure, which is a standard procedure⁶⁹. It has been recently reported that there are slight differences between the $1T'$ and $1T_d$ phases in monolayer TMDs³², with WTe_2 likely forming in the $1T_d$ phase. However, in this work we performed all calculations with the WTe_2 monolayer in the $1T'$ structure. Owing to very small differences between the $1T'$ and $1T_d$ phases, this assumption is appropriate. Full relaxations of the lattice parameters and ionic positions were performed on monolayer WSe_2 and WTe_2 in the $1H$ and $1T'$ phases using a $32 \times 32 \times 1$ and $32 \times 16 \times 1$ Γ -centered k -mesh, respectively, and a 500 eV plane-wave cutoff. The phonon band structures of these compounds were computed using density functional perturbation theory⁷⁰. Various chalcogen-alloyed compositions of the form $\text{WSe}_{2(1-x)}\text{Te}_{2x}$ were created by expanding these unit cells and substituting the appropriate amount of Te with Se (or vice versa). Full relaxations were again performed in each case, with the k -mesh

scaled appropriately to the size of the unit cell. In the case when multiple substitutional anions were needed to achieve a given composition, all combinations of the position of the alloying atoms relative to each other were tested, with the lowest energy configuration considered the ground state (Supplementary Fig. 12). The density of states was computed using the aforementioned PBE functional, as well as the HSE06 functional⁵⁶, with 25% Hartree-Fock exact exchange included.

Disclaimer. Certain commercial equipment, instruments, or materials are identified in this paper in order to specify the experimental procedure adequately. Such identification is not intended to imply recommendation or endorsement by the National Institute of Standards and Technology nor is it intended to imply that the materials or equipment identified are necessarily the best available for the purpose.

Data availability

The data that support the findings of this study are available from the corresponding author upon reasonable request.

Received: 19 July 2019; Accepted: 16 December 2019;

Published online: 15 January 2020

References

- Xu, X., Yao, W., Xiao, D. & Heinz, T. F. Spin and pseudospins in layered transition metal dichalcogenides. *Nat. Phys.* **10**, 343–350 (2014).
- Mak, K. F., Xiao, D. & Shan, J. Light-valley interactions in 2D semiconductors. *Nat. Photonics* **12**, 451–460 (2018).
- Schaibley, J. R. et al. Valleytronics in 2D materials. *Nat. Rev. Mater.* **1**, 16055 (2016).
- Žutić, I., Fabian, J. & Das Sarma, S. Spintronics: fundamentals and applications. *Rev. Mod. Phys.* **76**, 323–410 (2004).
- Splendiani, A. et al. Emerging photoluminescence in monolayer MoS_2 . *Nano Lett.* **10**, 1271–1275 (2010).
- Mak, K. F., Lee, C., Hone, J., Shan, J. & Heinz, T. F. Atomically thin MoS_2 : a new direct-gap semiconductor. *Phys. Rev. Lett.* **105**, 136805 (2010).
- Zeng, H., Dai, J., Yao, W., Xiao, D. & Cui, X. Valley polarization in MoS_2 monolayers by optical pumping. *Nat. Nanotechnol.* **7**, 490–493 (2012).
- Mak, K. F., He, K., Shan, J. & Heinz, T. F. Control of valley polarization in monolayer MoS_2 by optical helicity. *Nat. Nanotechnol.* **7**, 494–498 (2012).
- Jones, A. M. et al. Optical generation of excitonic valley coherence in monolayer WSe_2 . *Nat. Nanotechnol.* **8**, 634–638 (2013).
- Wang, G. et al. Valley dynamics probed through charged and neutral exciton emission in monolayer WSe_2 . *Phys. Rev. B* **90**, 075413 (2014).
- Hao, K. et al. Direct measurement of exciton valley coherence in monolayer WSe_2 . *Nat. Phys.* **12**, 677–682 (2016).
- Huang, J., Hoang, T. B. & Mikkelsen, M. H. Probing the origin of excitonic states in monolayer WSe_2 . *Sci. Rep.* **6**, 22414 (2016).
- Wang, G. et al. Control of exciton valley coherence in transition metal dichalcogenide monolayers. *Phys. Rev. Lett.* **117**, 187401 (2016).
- Chen, S.-Y. et al. Superior valley polarization and coherence of 2s excitons in monolayer WSe_2 . *Phys. Rev. Lett.* **120**, 046402 (2018).
- Ye, Z., Sun, D. & Heinz, T. F. Optical manipulation of valley pseudospin. *Nat. Phys.* **13**, 26–29 (2016).
- Tatsumi, Y., Ghalamkari, K. & Saito, R. Laser energy dependence of valley polarization in transition-metal dichalcogenides. *Phys. Rev. B* **94**, 235408 (2016).
- Yu, T. & Wu, M. W. Valley depolarization due to intervalley and intravalley electron-hole exchange interactions in monolayer MoS_2 . *Phys. Rev. B* **89**, 205303 (2014).
- Kioseoglou, G. et al. Valley polarization and intervalley scattering in monolayer MoS_2 . *Appl. Phys. Lett.* **101**, 221907 (2012).
- Miyauchi, Y. et al. Evidence for line width and carrier screening effects on excitonic valley relaxation in 2D semiconductors. *Nat. Commun.* **9**, 1–10 (2018).
- Shinokita, K. et al. Continuous control and enhancement of excitonic valley polarization in monolayer WSe_2 by electrostatic doping. *Adv. Funct. Mater.* **29**, 1900260 (2019).
- Xie, L. M. Two-dimensional transition metal dichalcogenide alloys: preparation, characterization and applications. *Nanoscale* **7**, 18392–18401 (2015).
- Duerloo, K.-A. N., Li, Y. & Reed, E. J. Structural phase transitions in two-dimensional Mo- and W-dichalcogenide monolayers. *Nat. Commun.* **5**, 4214 (2014).
- Rehn, D. A., Li, Y., Pop, E. & Reed, E. J. Theoretical potential for low energy consumption phase change memory utilizing electrostatically-induced structural phase transitions in 2D materials. *npj Comput. Mater.* **4**, 2 (2018).

24. Wang, X. et al. Potential 2D materials with phase transitions: structure, synthesis, and device applications. *Adv. Mater.* **1804682**, 1804682 (2018).
25. Duerloo, K.-A. N. & Reed, E. J. Structural phase transitions by design in monolayer alloys. *ACS Nano* **10**, 289–297 (2016).
26. Wang, G. et al. Spin-orbit engineering in transition metal dichalcogenide alloy monolayers. *Nat. Commun.* **6**, 10110 (2015).
27. Meng, Y. et al. Excitonic complexes and emerging interlayer electron–phonon coupling in BN encapsulated monolayer semiconductor alloy: $WS_{0.6}Se_{1.4}$. *Nano Lett.* **19**, 299–307 (2019).
28. Yun, S. J. et al. Tellurizing monolayer MoS_2 and WS_2 via alkali metal scooter. *Nat. Commun.* **8**, 2163 (2017).
29. Yu, P. et al. Metal-semiconductor phase-transition in $WSe_{2(1-x)}Te_{2x}$ monolayer. *Adv. Mater.* **29**, 1603991 (2017).
30. Lin, J. et al. Anisotropic ordering in 1T' molybdenum and tungsten ditelluride layers alloyed with sulfur and selenium. *ACS Nano* **12**, 894–901 (2018).
31. Rosenberger, M. R. et al. Nano-“squeegee” for the creation of clean 2D material interfaces. *ACS Appl. Mater. Interfaces* **10**, 10379–10387 (2018).
32. Xu, S. Y. et al. Electrically switchable Berry curvature dipole in the monolayer topological insulator WTe_2 . *Nat. Phys.* **14**, 900–906 (2018).
33. Castellanos-Gomez, A. et al. Deterministic transfer of two-dimensional materials by all-dry viscoelastic stamping. *2D Mater.* **1**, 011002 (2014).
34. del Corro, E. et al. Excited excitonic states in 1L, 2L, 3L, and bulk WSe_2 observed by resonant Raman spectroscopy. *ACS Nano* **8**, 9629–9635 (2014).
35. Zhao, W. et al. Lattice dynamics in mono- and few-layer sheets of WS_2 and WSe_2 . *Nanoscale* **5**, 9677 (2013).
36. Terrones, H. et al. New first order Raman-active modes in few layered transition metal dichalcogenides. *Sci. Rep.* **4**, 4215 (2015).
37. Luo, X. et al. Effects of lower symmetry and dimensionality on Raman spectra in two-dimensional WSe_2 . *Phys. Rev. B Condens. Matter Mater. Phys.* **88**, 1–7 (2013).
38. Sun, H. et al. Enhanced exciton emission behavior and tunable band gap of ternary $W(S_{1-x}Se_x)_2$ monolayer: temperature dependent optical evidence and first-principles calculations. *Nanoscale* **10**, 11553–11563 (2018).
39. Cuscó, R. et al. Temperature dependence of Raman scattering in ZnO . *Phys. Rev. B* **75**, 165202 (2007).
40. Ye, F. et al. Environmental instability and degradation of single- and few-layer WTe_2 nanosheets in ambient conditions. *Small* **12**, 5802–5808 (2016).
41. Jiang, Y. C., Gao, J. & Wang, L. Raman fingerprint for semi-metal WTe_2 evolving from bulk to monolayer. *Sci. Rep.* **6**, 19624 (2016).
42. Cao, Y. et al. Anomalous vibrational modes in few layer WTe_2 revealed by polarized Raman scattering and first-principles calculations. *2D Mater.* **4**, 035024 (2017).
43. Kim, Y. et al. Anomalous Raman scattering and lattice dynamics in mono- and few-layer WTe_2 . *Nanoscale* **8**, 2309–2316 (2016).
44. Duan, X. et al. Synthesis of $WS_{2x}Se_{2-2x}$ alloy nanosheets with composition-tunable electronic properties. *Nano Lett.* **16**, 264–269 (2016).
45. Fu, Q. et al. Synthesis and enhanced electrochemical catalytic performance of monolayer $WS_{2(1-x)}Se_{2x}$ with a tunable band gap. *Adv. Mater.* **27**, 4732–4738 (2015).
46. Mann, J. et al. 2-Dimensional transition metal dichalcogenides with tunable direct band gaps: $MoS_{2(1-x)}Se_{2x}$ monolayers. *Adv. Mater.* **26**, 1399–1404 (2014).
47. Feng, Q. et al. Growth of $MoS_{2(1-x)}Se_{2x}$ ($x = 0.41$ – 1.00) monolayer alloys with controlled morphology by physical vapor deposition. *ACS Nano* **9**, 7450–7455 (2015).
48. Jadcak, J. et al. Composition dependent lattice dynamics in MoS_xSe_{2-x} alloys. *J. Appl. Phys.* **116**, 193505 (2014).
49. Oliver, S. M. et al. The structural phases and vibrational properties of $Mo_{1-x}W_xTe_2$ alloys. *2D Mater.* **4**, 045008 (2017).
50. Kang, J., Tongay, S., Zhou, J., Li, J. & Wu, J. Band offsets and heterostructures of two-dimensional semiconductors. *Appl. Phys. Lett.* **102**, 012111 (2013).
51. Echeverry, J. P., Urbaszek, B., Amand, T., Marie, X. & Gerber, I. C. Splitting between bright and dark excitons in transition metal dichalcogenide monolayers. *Phys. Rev. B* **93**, 1–5 (2016).
52. Paur, M. et al. Electroluminescence from multi-particle exciton complexes in transition metal dichalcogenide semiconductors. *Nat. Commun.* **10**, 1709 (2019).
53. Tongay, S. et al. Defects activated photoluminescence in two-dimensional semiconductors: interplay between bound, charged and free excitons. *Sci. Rep.* **3**, 2657 (2013).
54. O'Donnell, K. P. & Chen, X. Temperature dependence of semiconductor band gaps. *Appl. Phys. Lett.* **58**, 2924–2926 (1991).
55. Perdew, J. P., Burke, K. & Ernzerhof, M. Generalized gradient approximation made simple. *Phys. Rev. Lett.* **77**, 3865–3868 (1996).
56. Heyd, J., Scuseria, G. E. & Ernzerhof, M. Hybrid functionals based on a screened Coulomb potential. *J. Chem. Phys.* **118**, 8207–8215 (2003).
57. Jin, C. et al. Interlayer electron–phonon coupling in WSe_2/hBN heterostructures. *Nat. Phys.* **13**, 127–131 (2017).
58. Chow, C. M. et al. Unusual exciton–phonon interactions at van der Waals engineered interfaces. *Nano Lett.* **17**, 1194–1199 (2017).
59. Tang, B. et al. Phase-controlled synthesis of monolayer ternary telluride with a random local displacement of tellurium atoms. *Adv. Mater.* **31**, e1900862 (2019).
60. Hanbicki, A. T. et al. Optical polarization of excitons and trions under continuous and pulsed excitation in single layers of WSe_2 . *Nanoscale* **9**, 17422–17428 (2017).
61. Konabe, S. Screening effects due to carrier doping on valley relaxation in transition metal dichalcogenide monolayers. *Appl. Phys. Lett.* **109**, 073104 (2016).
62. McCreary, K. M., Currie, M., Hanbicki, A. T., Chuang, H. J. & Jonker, B. T. Understanding variations in circularly polarized photoluminescence in monolayer transition metal dichalcogenides. *ACS Nano* **11**, 7988–7994 (2017).
63. Chakraborty, C., Mukherjee, A., Qiu, L. & Vamivakas, A. N. Electrically tunable valley polarization and valley coherence in monolayer WSe_2 embedded in a van der Waals heterostructure. *Opt. Mater. Express* **9**, 1479 (2019).
64. Qiu, L., Chakraborty, C., Dhara, S. & Vamivakas, A. N. Room-temperature valley coherence in a polaritonic system. *Nat. Commun.* **10**, 1–5 (2019).
65. Kresse, G. & Furthmüller, J. Efficiency of ab-initio total energy calculations for metals and semiconductors using a plane-wave basis set. *Comput. Mater. Sci.* **6**, 15–50 (1996).
66. Kresse, G. & Furthmüller, J. Efficient iterative schemes for ab initio total-energy calculations using a plane-wave basis set. *Phys. Rev. B Condens. Matter Mater. Phys.* **54**, 11169–11186 (1996).
67. Kohn, W. & Sham, L. J. Self-consistent equations including exchange and correlation effects. *Phys. Rev.* **140**, A1133–A1138 (1965).
68. P.E., B. Projector augmented-wave method. *Phys. Rev. B* **50**, 17953–17979 (1994).
69. Xiang, H. et al. Quantum spin Hall insulator phase in monolayer WTe_2 by uniaxial strain. *AIP Adv.* **6**, 095005 (2016).
70. Baroni, S., Giannozzi, P. & Testa, A. Green's-function approach to linear response in solids. *Phys. Rev. Lett.* **58**, 1861–1864 (1987).

Acknowledgements

P.M.V. and S.M.O. acknowledge support from the National Science Foundation (NSF) under Grant No. DMR-1748650, the George Mason University Quantum Materials Center, and the George Mason University Presidential Scholars Program. J.Y. was supported by funds from Binghamton University. Computational resources were provided by the Department of Defense High Performance Computing Modernization Program. S.K. acknowledges support from the US Department of Commerce, NIST under financial assistance award 70NANB18H155. T.L.R. was supported by the Office of Naval Research.

Author contributions

P.M.V. and S.M.O. conceived and designed the experiments and wrote the manuscript with input from all coauthors. S.M.O. prepared van der Waals heterostructures and carried out all experiments. A.V.D. and S.K. grew the bulk crystals used in this work. J.Y. and T.L.R. performed the density functional theory calculations.

Competing interests

The authors declare no competing interests.

Additional information

Supplementary information is available for this paper at <https://doi.org/10.1038/s42005-019-0277-7>.

Correspondence and requests for materials should be addressed to P.M.V.

Reprints and permission information is available at <http://www.nature.com/reprints>

Publisher's note Springer Nature remains neutral with regard to jurisdictional claims in published maps and institutional affiliations.



Open Access This article is licensed under a Creative Commons Attribution 4.0 International License, which permits use, sharing, adaptation, distribution and reproduction in any medium or format, as long as you give appropriate credit to the original author(s) and the source, provide a link to the Creative Commons license, and indicate if changes were made. The images or other third party material in this article are included in the article's Creative Commons license, unless indicated otherwise in a credit line to the material. If material is not included in the article's Creative Commons license and your intended use is not permitted by statutory regulation or exceeds the permitted use, you will need to obtain permission directly from the copyright holder. To view a copy of this license, visit <http://creativecommons.org/licenses/by/4.0/>.

© The Author(s) 2020